



HELSINKI UNIVERSITY OF TECHNOLOGY

Faculty of Electronics, Communications and Automation

Department of Micro and Nanosciences

Zhen Zhu

OPTICAL AND STRUCTURAL CHARACTERIZATION OF
InGaN/GaN MULTIPLE QUANTUM WELL STRUCTURES
IRRADIATED BY HIGH ENERGY HEAVY IONS

Master's Thesis submitted in partial fulfillment of the requirements of
the degree of Master of Science in Technology.

Espoo, Finland, 08.12.2008

Supervisor: Docent Markku Sopanen

Instructor: M.Sc. Muhammad Ali

Preface

This thesis was carried out in Department of Micro and Nanosciences at Helsinki University of Technology (TKK).

First I would like to express my deep gratitude to Professor Harri Lipsenen for giving me a chance to work in the laboratory. I am further indebted to Docent Markku Sopanen for supervising my work. And I also want to thank my instructor Muhammad Ali for his guidance and support.

Additionally, I would like to thank Aierken, olli, Sami, Shuo, Ya, Jie, Gintare, Teemu, Alex and all the staff members of the Micro and Nanosciences Laboratory who provided knowledge and support.

Finally, I wish to thank my parents and friends, especially my fiancée Cuiwen. Their persistent love and support has given me the strength to persevere in reaching my educational goals.

Zhen Zhu, Espoo

December 2008

Author:	Zhen Zhu	
Title of Thesis:	Optical and Structural Characterization of InGaN/GaN Multiple Quantum Well Structures Irradiated by High Energy Heavy Ions	
Date:	08.12.2008	Pages: 46
Faculty:	Electronics, Communications and Automation	
Department:	Micro and Nanosciences	
Professorship:	Optoelectronics	Code: S-104
Supervisor:	Docent Markku Sopanen	
Instructor:	M. Sc. Muhammad Ali	
<p>This topic is a cooperation project between Helsinki University of Technology (TKK) and Uppsala University (UU). Multiple quantum wells (MQWs) were grown and characterized in Department of Micro and Nanosciences of TKK. The samples were irradiated in Ångström Laboratory of UU.</p> <p>In this thesis, quantum well (QW) structures based on InGaN/GaN material system have been grown by using metalorganic vapor phase epitaxy (MOVPE). The samples grown had 5 and 10 quantum wells with 6 and 10% of indium, respectively. Iodine and bromine have been used as irradiations ions. The irradiation fluences of these ions were varied from 10^9 to 10^{12} ions/cm².</p> <p>Our X-ray diffraction results have shown no signs of a major crystal damage on the quantum wells. The photoluminescence results indicate a strong dependence of the optical properties on the type and fluence of ions used for irradiation.</p>		
Keywords:	gallium nitride, indium gallium nitride, metalorganic vapor phase epitaxy, multiple quantum well, x-ray, photoluminescence, irradiation, fluence	

Contents

1	Introduction.....	1
2	Basic Semiconductor Theory	3
2.1	Semiconductor materials	3
2.2	The band theory	4
2.3	Crystal structure	7
2.4	Quantum wells	8
3	Gallium Nitride	10
3.1	Crystal structure of GaN	10
3.2	Energy band of GaN.....	12
4	Experimental Methods	14
4.1	Metalorganic vapor phase epitaxy.....	14
4.2	Radiation	16
4.2.1	Radiation effects on semiconductors.....	16
4.2.2	Particle types	18
4.2.3	Light and heavy ions	18
4.2.4	Radiation for LED materials	19
4.3	Measurement methods.....	19
4.3.1	X-ray diffraction.....	20
4.3.2	Photoluminescence	21
5	Results and Discussion.....	25
5.1	Growth of InGaN/GaN multiple quantum wells	25
5.2	Irradiation by heavy ions.....	27
5.3	XRD results	28

5.4	Continuous wave photoluminescence results.....	30
5.4.1	CW-PL results of samples irradiated by I^{9+} ions	30
5.4.2	CW-PL results of samples irradiated by Br^{3+} ions.....	33
5.5	Low temperature photoluminescence results	35
5.5.1	Activation energy	35
5.5.2	Internal quantum efficiency.....	39
5.6	Time resolved photoluminescence at room temperature.....	41
6	Summary	43
	Appendix 1	45
	Appendix 2	46
	References	47

1 Introduction

Gallium nitride (GaN) is an important group III-V compound semiconductor having the wurtzite crystal structure with a direct and wide bandgap of 3.4 eV. It is considered as one of the most promising semiconductor material for visible light emitters at present. GaN based optoelectronics product development has turned into a hot research field and is at the forefront of semiconductor research and development in the world. GaN based visible light emitting diodes (LEDs) and laser diodes (LDs) are already commercialized for a variety of lighting and data storage applications. In addition, this material system has also shown promise for microwave, high-power and high frequency devices. Also, ultraviolet (UV) light detection is a very important technological application [1].

InGaN/GaN multiple quantum well (MQW) structures emitting at 410 nm and 460 nm were grown using the metal-organic vapor phase epitaxy (MOVPE) facility in Micronova, Finland. The irradiation facility at the Ångström Laboratory of Uppsala University in Sweden was utilized to irradiate the quantum well samples. Iodine (I^{9+}) and bromine (Br^{3+}) ions were used for the irradiation of the quantum wells. Two key techniques, that is X-ray diffraction (XRD) and photoluminescence (PL) were employed to study the effect of ion bombardment. All characterization of the samples was performed using the facilities available in Micronova.

This thesis is organized as follows. Chapter 2 and Chapter 3 focus on the basic properties of semiconductors and the details of the GaN material system. In Chapter 4,

various experimental methods used in this thesis are discussed. Some details of the epitaxial growth and the theory related to irradiation of semiconductors are explained. In the last few sections the XRD and PL characterization techniques employed in this thesis are explained. In Chapter 5 the results obtained from the various irradiated samples are shown and discussed. The chapter investigates the effect of different bombardment ions and radiation fluences on the quantum wells under study. Finally, the last chapter highlights the conclusions obtained from this research.

2 Basic Semiconductor Theory

This chapter gives a basic overview of the physics of semiconductors related to this thesis. The aim of this chapter is to help the reader in understanding the fundamentals of both semiconductors and crystal structures.

2.1 Semiconductor materials

The study of semiconductor materials began in the early nineteenth century [2]. Right now, the semiconductors have become tremendously important materials in industry. They have conductivities between the metals and the insulators. Table 2-1 shows the portion of the periodic table related to semiconductors. For example, the most important elemental semiconductors in the group IV are Si and Ge. Table 2-2 shows some common compound semiconductor materials, most of which are combinations of the elements which come from the groups III and V.

Period	Column II	III	IV	V	VI
2		B	C	N	O
		Boron	Carbon	Nitrogen	Oxygen
3	Mg	Al	Si	P	S
	Magnesium	Aluminum	Silicon	Phosphorus	Sulfur
4	Zn	Ga	Ge	As	Se
	Zinc	Gallium	Germanium	Arsenic	Selenium
5	Cd	In	Sn	Sb	Te
	Cadmium	Indium	Tin	Antimony	Tellurium
6	Hg		Pb		
	Mercury		Lead		

Table 2-1. Portion of the periodic table related to semiconductors [3].

AlAs	Aluminium Arsenide
GaP	Gallium Phosphide
GaAs	Gallium Arsenide
InP	Indium Phosphide
GaN	Gallium Nitride
InGaN	Indium Gallium Nitride
AlGaAs	Aluminium Gallium Arsenide

Table 2-1. List of some common compound semiconductors.

2.2 The band theory

In solids there are two distinct energy bands which are important for electrical conductivity. One is called the valence band in which electrons fully occupy the lowest energy state at 0 K, and the other is known as the conduction band which will be empty at 0 K. The behavior of a solid as a conductor, a semiconductor or an insulator depends on whether the conduction band is completely filled, partially filled or almost empty. The band gap energy E_g can be defined by

$$E_g = E_c - E_v, \quad (2.1)$$

where E_c is the lowest energy of the conduction band and E_v is the highest energy of the valence band.

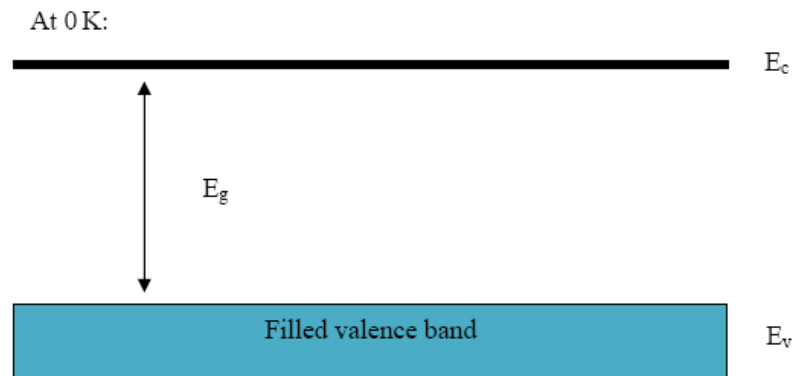


Figure 2-1. Energy bandgap is between the valence and conduction bands at 0 K.

In a conductor, the uppermost band is partially filled, there are many electrons that can easily move in real space and keep within the conduction band. However, the conduction band of the insulator is almost empty. The band gap between the valence band and the conduction band is very large. This energy is considerably larger than the additional kinetic energy which may be given to an electron through the application of an electric field. Electrons, therefore, are locked into the filled energy bands and cannot carry current even with an applied electric field [4].

A semiconductor has an intermediate bandgap (typically around 1 eV). Different possibilities of band arrangements in the solids have been shown in Figure 2-2. At a finite temperature a semiconductor has more electrons in the conduction band and holes in the valence band than an insulator, so it conducts better. On the other hand, the conductivity is nowhere near to that of a conductor.

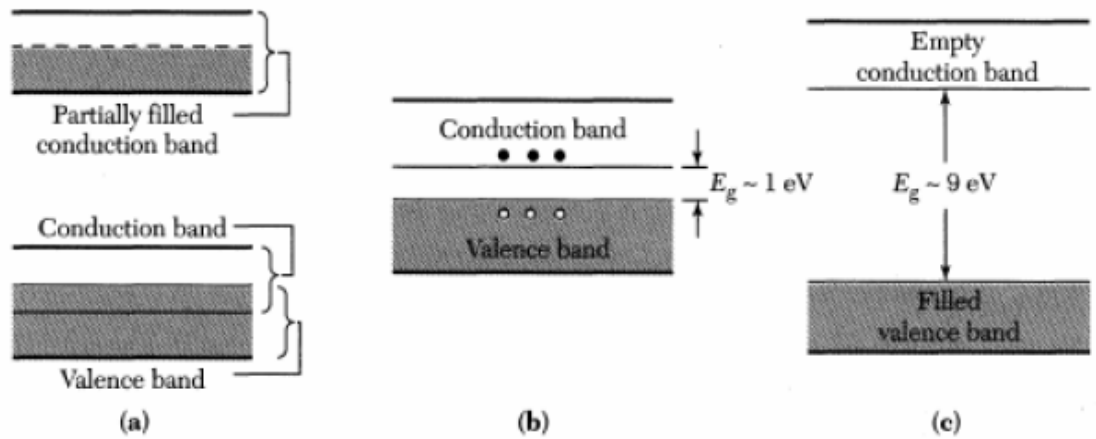


Figure 2-2. Schematic illustration of energy bands in (a) a conductor with two possibilities (either the partially filled conduction band shown at the upper portion or the overlapping bands shown at the lower portion), (b) a semiconductor, and (c) an insulator [3].

In semiconductor materials, two kinds of bandgaps can be observed. One is a direct band gap, another is an indirect band gap. Figure 2-3 (a) shows the band structure of a semiconductor with a direct bandgap. In the case of the direct band gap, the maximum of the valence band E_v is directly located below the minimum of the conduction band E_c in the k -space (k is wave vector). In a direct band gap semiconductor, the electrons from the conduction band minimum can combine directly with the holes at the valence band maximum, while conserving the momentum. The energy of the recombination across the bandgap is emitted in the form of a photon. Semiconductors such as GaAs, InP, InGaAs, GaN *etc.* are examples of direct bandgap semiconductors [5]. Figure 2-3 (b) shows the band structure of an indirect semiconductor. An indirect bandgap is a band gap in which the energy minimum of the conduction band is shifted by a k -vector from the valence band maximum. Since the different k -vectors represent the difference in momentum, it makes the recombination of electrons to the valence band a second-order process. That is why indirect bandgap materials, such as silicon carbide, are inefficient at emitting light.

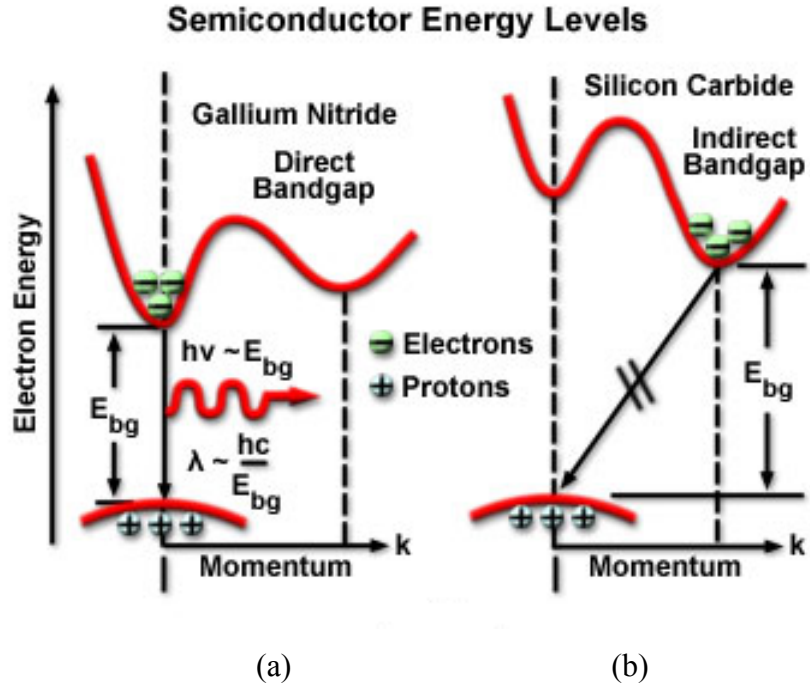


Figure 2-3. Band structure of (a) a direct semiconductor and (b) an indirect semiconductor [6].

2.3 Crystal structure

In a crystal, the atoms are arranged in a regular pattern that repeats throughout the material. The periodic arrangement of atoms in a crystal is called a lattice [3]. All the lattice points are geometrically equivalent. A lattice therefore exhibits perfect translational symmetry and, relative to an arbitrarily chosen origin, at a lattice point, any other lattice point has the position vector [7]

$$\mathbf{r}_{123} = n_1\mathbf{a} + n_2\mathbf{b} + n_3\mathbf{c} , \quad (2.2)$$

where n is necessarily an integer and the vectors \mathbf{a} , \mathbf{b} and \mathbf{c} are fundamental units of the translational symmetry. There are fourteen different lattice structures which are called the *Bravais* lattices. Figure 2-4 shows the three most important cubic lattice structures.

Simple cubic (SC) lattice has one lattice point at each of the eight corners of the cube. In the body centered cubic (BCC) lattice, there is one lattice point at each corner of the cube and one lattice point in the center of the cube. For face centered cubic (FCC) lattice, there is one atom at each corner and one atom in each face of the cube.

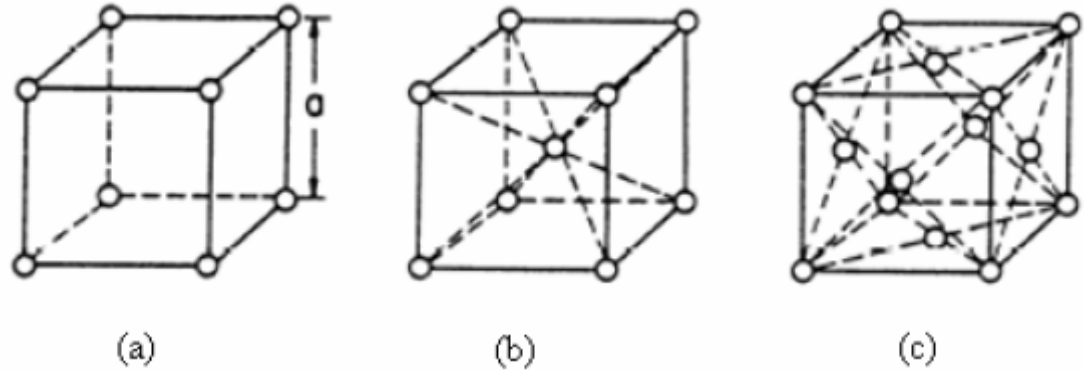


Figure 2-4. Three cubic crystal unit cells: (a) simple cubic (SC), (b) body centered cubic (BCC) and (c) face centered cubic (FCC) [8].

2.4 Quantum wells

With advances in fabrication techniques of microscopic structures in recent decades, the physics of quantum wells has assumed a major role in modern technology. A quantum well is a thin layer which can confine electrons and holes in the dimension perpendicular to the layer surface, while the movement in the other dimensions is not restricted. Both electrons and holes see lower energy in the ‘well’ layer [9].

The effects of quantum confinement take place when the quantum well thickness becomes comparable to the *de Broglie* wavelength of the carriers (generally electrons and holes), leading to energy levels called ‘energy sub-bands’, *i.e.*, the carriers can only have discrete energy values in the direction perpendicular to the layer. These so called quantization effects result in the allowed energy bands whose energy positions are dependent on the height and width of the barrier [10]. Optical transitions in a quantum well can occur either between the conduction and the valence band (inter-band

transition) or within the conduction band (inter-sub-band transition) as shown in Figure 2-5.

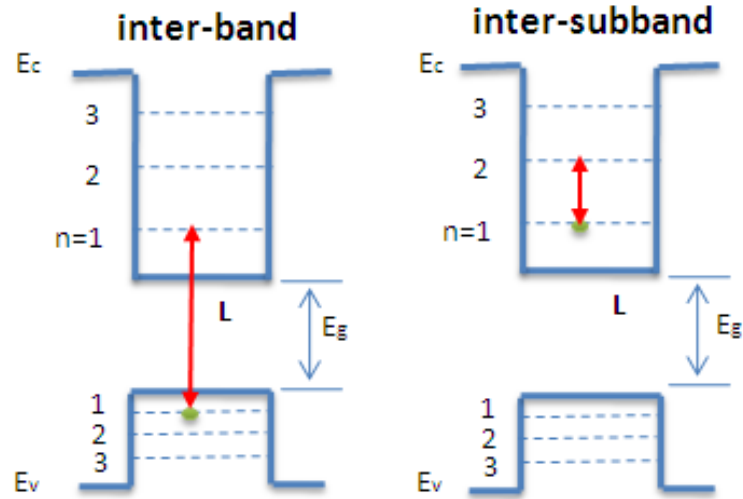


Figure 2-5. Optical inter-band and inter-sub band transitions in a quantum well.

Quantum wells can be fabricated by forming heterojunctions between different semiconductors. From an electronic viewpoint, the semiconductors are different because they have different band structures. Of course, there are many other properties which are also different, such as dielectric constant, the lattice constant and the effective mass [11]. Typically, the quantum wells are grown by epitaxy and usually a lattice mismatch between the two different materials is produced.

3 Gallium Nitride

Recent years have shown the need for high-efficiency optoelectronic materials. Therefore, research and development in optoelectronics technology has boomed. The compound semiconductor materials offer the advantage of high luminous performance. Especially, group III-N materials are particularly suitable for ultra violet, blue and green light emitting devices. This chapter gives a basic overview of the crystalline structure and the properties of GaN.

3.1 Crystal structure of GaN

GaN can have two lattice structures. It can be either hexagonal wurtzite (α -GaN) or cubic zinc blende (β -GaN). The wurtzite structure is the most widely used form of GaN. The crystal structure of the GaN layers used in this thesis is also the wurtzite. Therefore, some of the properties of such a structure are described below.

Wurtzite structure of GaN is a symmetrical hexagonal structure and consists of tetrahedrally coordinated gallium and nitrogen atoms that are stacked in an ABABAB... pattern. Figure 3-1 shows the wurtzite structure of GaN, where c and a are two lattice parameters, u is the dimensionless parameter which characterizes the bond aligned along the main axis. The parameter u is measured in units of the c-axis lattice parameter, and provides information about the distortion in the unit cell [12].

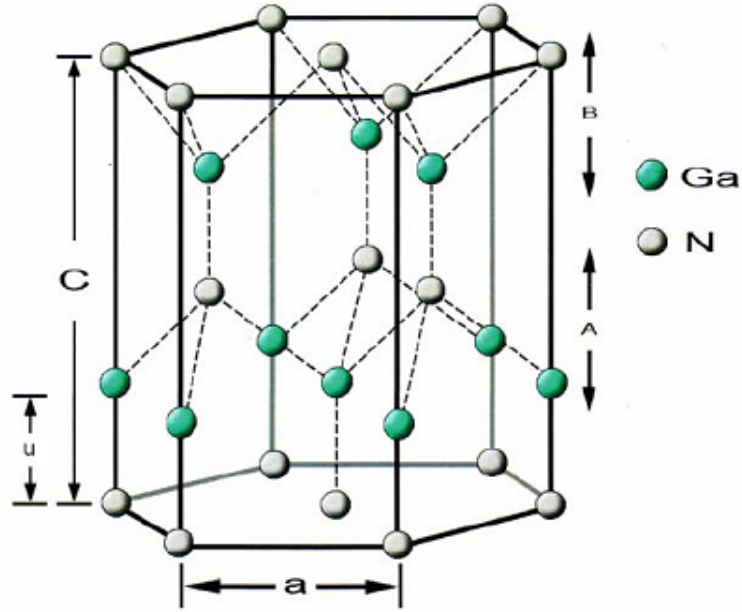


Figure 3-1. Hexagonal wurtzite structure of GaN [13].

There are two possibilities to deviate from the ideal wurtzite structure ($c/a = 1.633$ and $u = 0.375$), *i.e.*, by changing the c/a ratio or by changing the u value [14]. Such deviations are often observed in wurtzite type structures [15] but there exists a strong correlation between the c/a ratio and the u parameter. If the c/a decreases, then u increases in such a way that the four tetrahedral distances remain nearly constant and the tetrahedral angles are distorted [16]. The bond lengths would be equal if [14]

$$u = \frac{1}{3} \times \frac{a^2}{c^2} + \frac{1}{4} . \quad (3.1)$$

Table 3-1 shows the structural parameters of GaN, AlN and InN. For GaN, the wurtzite structure is nearly ideal.

Lattice Parameter	GaN	AlN	InN
a	3.174 Å	3.091 Å	3.538 Å
c	5.169 Å	4.954 Å	5.707 Å
u	0.3786 Å	0.3815 Å	0.3792 Å
c/a	1.627	1.601	1.612

Table 3-1. Lattice parameters for common III-N compounds [17].

3.2 Energy band of GaN

GaN is a direct band gap semiconductor material, and it has a band gap energy of about 3.48 eV. Figure 3-2 shows the bandgap energy of the three different III-nitride (III-N) materials (AlN, GaN and InN) as a function of lattice constant.

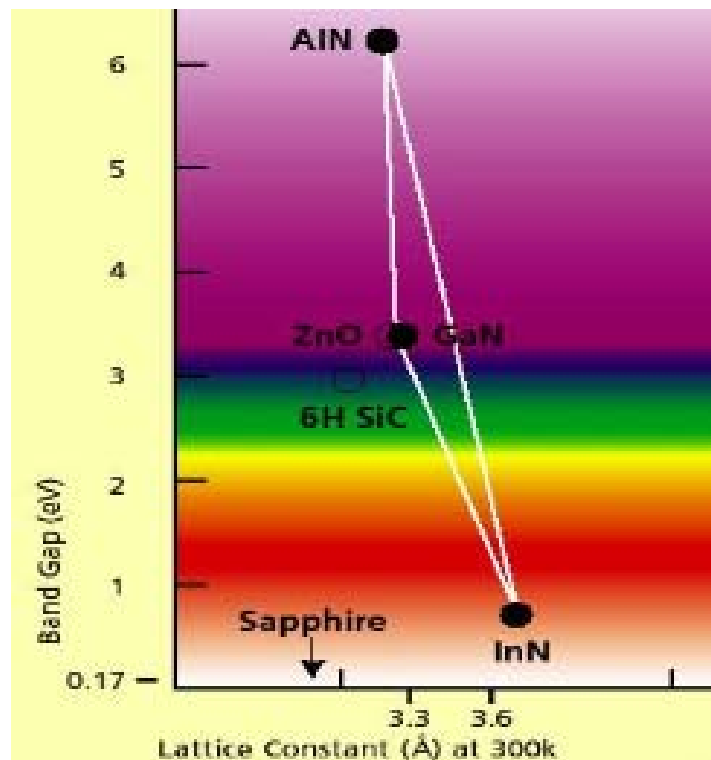


Figure 3-2. Bandgap energy vs. lattice constant of InN, GaN and AlN [18].

As Figure 3-2 shows, if InN is alloyed into GaN, the bandgap will be decreased. On the other hand, the GaN bandgap can be increased by alloying with AlN. For this reason, this III-N system has a very broad range of band gap values from 0.7 to 6.1 eV. Thus, a wide span of emission wavelengths (from 200 to 1378 nm) covering the entire visible spectra and extending into the infrared and ultraviolet areas can be achieved [9].

4 Experimental Methods

This chapter discusses the experimental methods used in this thesis. Firstly, a brief overview of the fabrication technique of the samples used for our research is presented. The next section highlights the method used for the irradiation of quantum wells. The last part of the chapter discusses the measurement techniques used in this work.

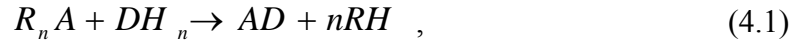
4.1 Metalorganic vapor phase epitaxy

There are several ways for fabricating epitaxial layers of III-nitrides such as liquid phase epitaxy (LPE), molecular beam epitaxy (MBE), hydride vapor phase epitaxy (HVPE) and metalorganic vapor phase epitaxy (MOVPE). In our study, all the samples were fabricated by MOVPE, so only this method will be introduced.

Metalorganic vapor phase epitaxy (MOVPE) is a chemical vapor deposition method of epitaxial growth, especially for compound semiconductors from organic compounds or metalorganics and metal hydrides containing the required chemical elements.

The MOVPE process starts with a gas mixture which contains the molecular compounds, termed precursors (necessary for growth), and a carrier gas. The latter is usually hydrogen, with an operating pressure between 7.5 Torr and atmospheric pressure (760 Torr). The chemical reactions take place inside a chamber which contains a heated substrate. Close to this substrate, the precursors are ‘cracked’ (*i.e.*,

decomposed), which leads to a series of chemical reactions between the reactive species created by the cracking process. The result of these reactions is the deposition of a thin film on the substrate. The simplest case involves a pyrolysis reaction of vapors of a volatile metalorganic (MO) compound and a gaseous hydride, given by [19]



where R is an organic radical of some unspecified form but generally of low order, such as methyl- or ethyl-radical, and A and D are the constituent species for the deposited solid. There are a number of reactions of the group III and V source molecules as well as growth related surface processes such as the adsorption or desorption of chemical species and surface migration. A schematic overview of such processes is shown in Figure 4-1. For reasons of uniform deposition low pressures are preferred. This is a consequence of the more laminar flow pattern and the more homogeneous temperature field within the reactor.

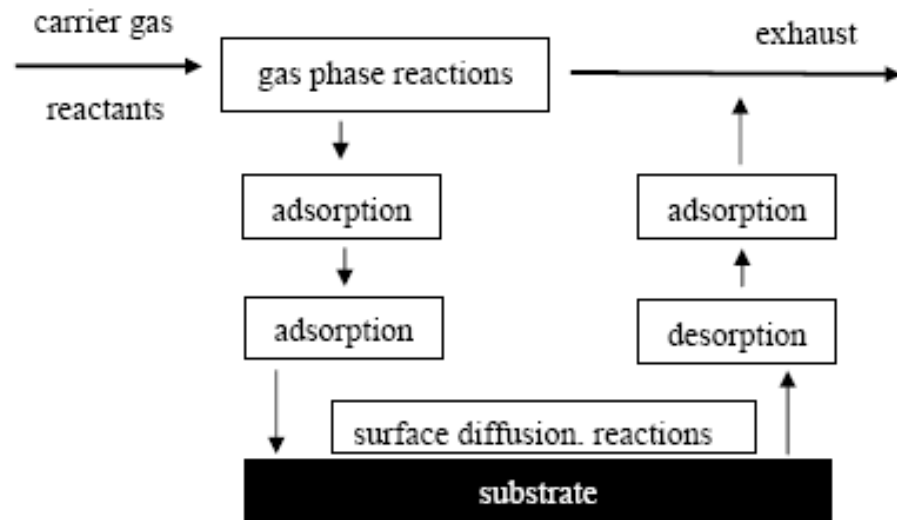


Figure 4-1. Schematic illustration of the basic processes of MOVPE.

The MOVPE growth process consists of many parallel and serial reaction steps occurring simultaneously. For serial reactions, the slowest step controls the overall reaction rate. For parallel reactions, the overall reaction rate is the sum of the individual reaction rates, hence the fastest reaction controls the overall reaction rate [20].

In a MOVPE systems, the most important elementary steps determining the overall reaction rate is controlled by an interplay between thermodynamics, kinetics and hydrodynamics of the processes. The thermodynamics of growth describes the driving force for the overall growth process by indicating in which direction the reactions will proceed and predicting the solid stoichiometry [20]. Kinetics controls the rate at which the possible gas phase and surface reactions occur [21]. The hydrodynamics of the process controls the mass transport of the molecules in the gas phase, the temperature distribution, the velocity profile and the total pressure in the reactor [20].

4.2 Radiation

Generally speaking, radiation is all around us. There are, however, different types of radiation, some coming from natural sources and some which is created by humans. The amount of radiation that semiconductor devices and materials encounter during their lifecycle strongly depends on the radiation environments and their operating conditions. For example, in space missions it is obvious that there is a radiation-harsh environment. However, also during the fabrication process and even for standard terrestrial operation, the devices may suffer from ionizing radiation [22].

4.2.1 Radiation effects on semiconductors

A semiconductor device in a radiation environment is generally subjected to a mix of particles, with quite a range of energies. When an energetic particle travels through a solid state system, it may lose its energy in various ways, thereby creating various types of defects. In this section, the ionization and displacement damage will be introduced.

Ionization damage is the dominant mechanism when energetic particles interact with solid-state matter. Ionization ability depends on the energy of the impinging individual particles, and not on their number. A large flood of particles generally will not cause ionization if these particles do not carry enough energy to be ionizing. The passage of the ionizing radiation through matter can be effectively studied by considering both electromagnetic radiation with photons from γ or x-rays and heavy and light charged particles.

Semiconductor devices operated in a radiation environment such as in space must exhibit the high-radiation hardness due to high-energy radiation. When a high-energy particle traverses a semiconductor device, the energy transferred during an elastic or inelastic nuclear collision maybe large enough to knock some atoms from their lattice site. The knock-on atoms primarily create Frenkel defects which are pairs of point defects close enough to exhibit an interaction: vacancy and an atom in an interstitial position. For collisions hard enough to allow large energy transfer, the knock-on atoms can collide with other atoms, creating more vacancies and interstitial atoms. When these defects are closely space, a cluster of defects can be created. The presence of such defects produce changes in the properties of the semiconductor [23].

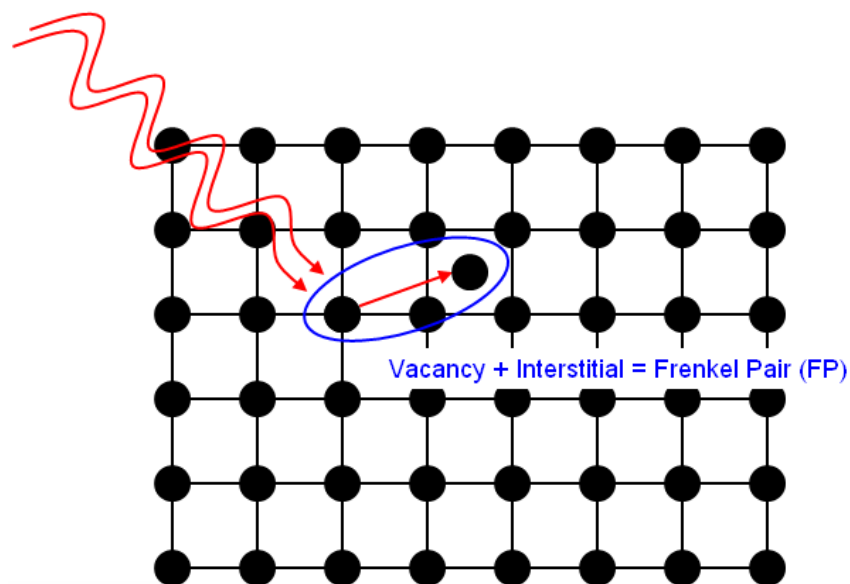


Figure 4-2. Diagram of displacement damage [24].

In general, any disturbance of the lattice periodicity may give rise to energy levels in the bandgap. The radiation induced defects have a major impact on the electrical and optical behavior of semiconductor materials and devices [25].

4.2.2 Particle types

The constituent particles that compose of the radiation fields previously described can be classified as either photons, neutrons or charged particles. Photons can be from γ or x-rays, which are capable of interacting with the material via the photoelectric effect. The neutron interaction is generated by elastic and inelastic scattering. And the charged particles consist of electrons, protons, and light/heavy ions. They are able to interact via Rutherford scattering or nuclear interactions depending on their mass [26].

4.2.3 Light and heavy ions

It is common knowledge that the charged particles can be distinguished by mass. Light or heavy ions refer to an ionized atom which is usually lighter or heavier than helium. Ion reactions are often used to produce intense neutron sources. The light ions are often the projectiles of choice for this purpose. This is because in certain cases at least one neutron may be quite loosely bound in the projectile, for example, the binding energy of the deuteron is only 2.2 MeV, which could be compared with a value of 6 to 8 MeV for heavy mass nuclei [27]. Both light-ion irradiation and heavy-ion irradiation produce point defects, but the resultant defect morphology is quite different [28]. A light ion is expected to create isolated point defects, whereas a heavy ion tends to yield clusters of point defects [29, 30, 31, 32].

4.2.4 Radiation for LED materials

Modern LEDs are often based on III-V group materials with quantum well structures for example the GaN/InGaN/GaN system is shown in Figure 4-3. There have been a few studies conducted on the impact of radiation on GaN and its related alloys, most of which have been performed on either GaAs or its related alloys. It has been shown that irradiation changes the optical absorption, the refractive index, the photoluminescence, and the photoconductivity of III-V materials. However, in the case of MQW structures ion damage may be used beneficially to produce so-called quantum well intermixing (QWI), which provides an elegant method for local bandgap engineering of a LED [22]. On the other hand, the non-radiative damage centers may be doubled, thus deteriorating the properties of LED devices.

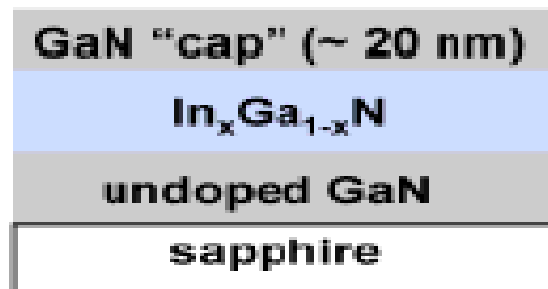


Figure 4-3. Schematic of the GaN/InGaN/GaN structure [33].

4.3 Measurement methods

To investigate the effect of radiation on the quantum wells, X-ray diffraction (XRD) and photoluminescence (PL) studies have been performed on the samples.

4.3.1 X-ray diffraction

X-rays are invisible, but they travel in straight lines and affect a photographic film in the same way as ordinary visible light. In 1912, X-ray diffraction (XRD) by crystals was discovered, and this discovery simultaneously proved the wave nature of X-rays and provided a new method for investigating the fine structure of matter [34]. In XRD, X-rays are reflected from adjacent crystal planes separated by a distance when the path difference between them is an integer multiple of the wavelength used. This condition is known as the Bragg's law

$$2d \sin \theta = n\lambda , \quad (4.2)$$

where d is the distance between the two neighboring lattice planes, θ is the Bragg angle, n is an integral number which describes the order of reflection and λ is the wavelength of the X-rays.

In this work a high-resolution X-ray diffraction (HR-XRD) system was used. The system is a Philips X'Pert Pro diffractometer, which can be operated in three axis configuration. Figure 4-4 shows the schematic illustration of the XRD setup. In this setup an analyzer crystal is located in front of the detector in the diffracted beam path to improve the angular resolution. A four crystal germanium monochromator is used to select the $Cu - K\alpha_1$ line ($\lambda = 1.541 \text{ \AA}$) from the emission spectrum of the X-ray tube [35]. An X-ray mirror is placed in front of the monochromator that is used to reduce the divergence of the incident beam.

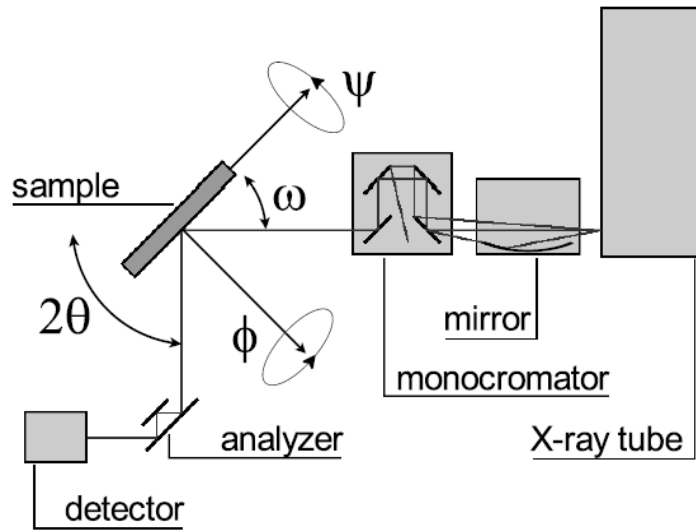


Figure 4-4. Schematic illustration of the high-resolution X-ray diffraction setup.

The compositional analysis can be done by using the rocking curve scans. In a rocking curve scan the sample is moved over a very small angular range. The graphs can be intensity *vs.* ω or intensity *vs.* $\omega - 2\theta$. The XRD curve obtained from the samples was analyzed by a simulation software to achieve the thickness of the barrier layer and the individual composition of the different elements in quantum wells layers.

4.3.2 Photoluminescence

Photoluminescence (PL) spectroscopy provides one of the most useful methods to investigate the optical quality of heterostructures [36]. The PL spectra provide the transition energies, which can be used to identify the electronic energy levels. In a quantum mechanical field, a PL process can be described as an excitation of carriers to a higher energy state and then a return to a lower energy state resulting in photon emission. PL is a simple, versatile, and non-destructive technique, however, the fundamental limitation of PL analysis is its dependence on radiative events. Materials with poor radiative efficiency are difficult to study via common PL.

When continuous wave (CW) excitation is used in a PL experiment, the system quickly converges to the steady state. The rate of excitation is the same as the rate of recombination, and the photo-generated carrier density is constant in time. In contrast, when the excitation is caused by a series of short laser pulses, the density of carriers depends on time. The laser pulse can be much shorter than the recombination time, so a specific carrier concentration can be generated almost instantaneously. For this reason, time-resolved photoluminescence (TR-PL) can be helpful in determining carrier lifetimes and to identify and characterize various recombination mechanisms in the material [37].

The setup of continuous wave PL is very simple, including an optical source (pump laser), a spectrophotometer and an optical fiber. Figure 4-5 shows the schematic of the CW-PL setup used in this thesis. A He-Cd laser with a maximum power of 0.02 W at 325 nm was used as the excitation source. A set of mirrors and lenses was used to align and focus the laser beam onto the samples. The PL coming out of the sample was collected and fed to a spectrometer via an optical fiber.

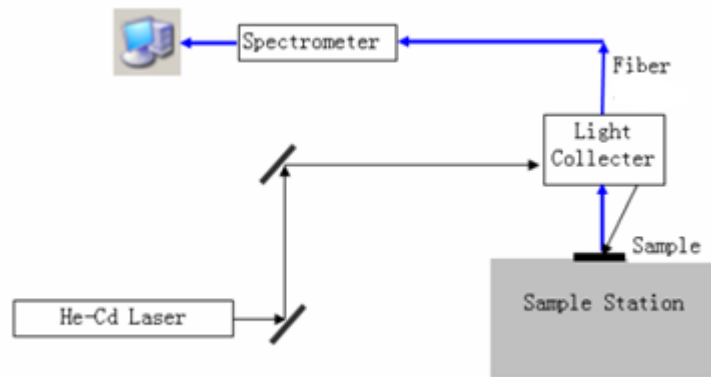


Figure 4-5. Diagram of the basic CW-PL setup used in this work.

In addition, the PL intensity at different temperatures can be used to further characterize the underlying electronic states and energy bands in the material [38]. At the lowest temperature, the radiative recombination is a dominant phenomenon. With increasing temperature the radiative recombination decreases. In contrast, the non-radiative recombination processes tend to increase with the rising temperature. Based on the

theories of PL temperature dependence, a low temperature PL (LT-PL) measurement has been carried out. Figure 4-6 shows the setup which was built for the LT-PL measurements performed in this thesis.

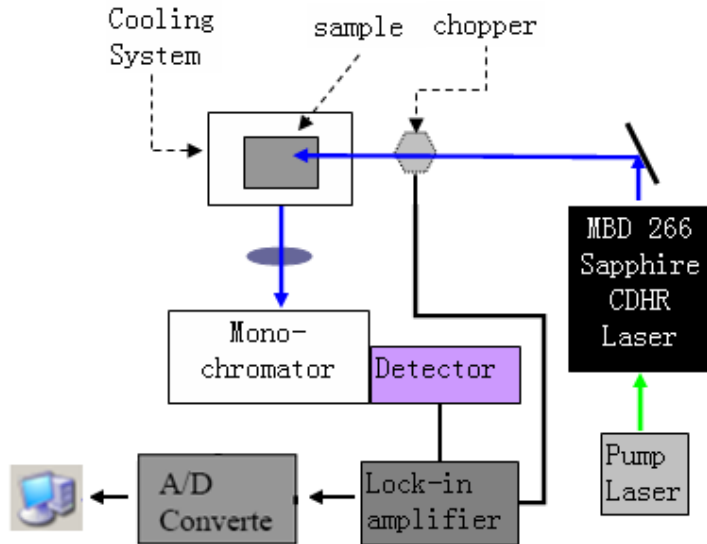


Figure 4-6. Low temperature PL system setup.

A Nd-Yag laser with a power of 6 watts was used to pump the Coherent MBD 266 cavity laser. The wavelength of the laser beam achieved using this setup was 266 nm. The laser beam was directed to hit the samples using an arrangement of mirrors and lenses. The samples were placed inside a cryostat so that low temperature measurements could be performed. Different PL intensities from samples were collected as the temperature was varied between 300 and 15 K. Standard lock-in techniques were used to amplify the signal from the detector.

Compared to the basic CW-PL setup, the setup of time resolved PL is more complex. The components in this system were a laser, mirrors, lenses, a nonlinear crystal, a monochromator and a detector. The layout of the TR-PL setup is shown in Figure 4-7. The Ti:Sapphire laser was pumped by a Nd-Yag laser (at 8 watt). A laser at a wavelength of 800 nm with 1W of power hit the BIBO crystal (BiB_3O_6) at a specified point. Due to the nonlinear effect, the laser frequency was doubled and the wavelength changed to around 400 nm. This pulsed laser at 400 nm was used as a source to excite

the InGaN/GaN quantum wells emitting at 460 nm. The emitted photons were collected by the detector and photon-counting electronics was used to create the time-resolved curve.

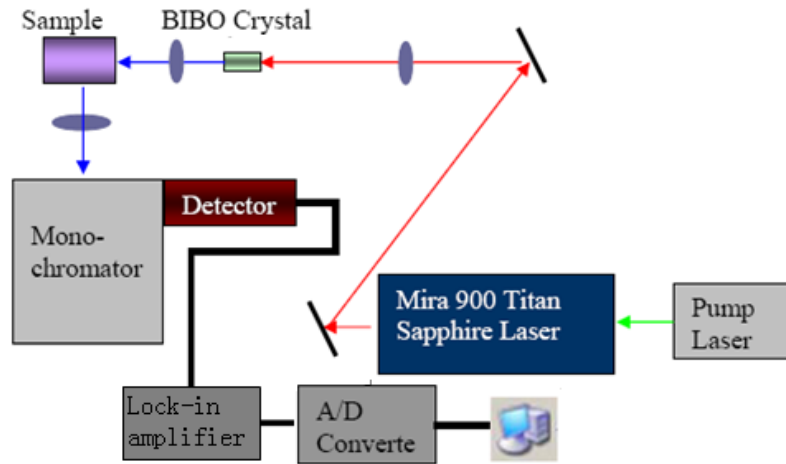


Figure 4-7. Diagram of the TR-PL setup used in this work.

5 Results and Discussion

Section 5.1 of this chapter explains the growth conditions of the samples used in this study. Section 5.2 discusses the irradiation by heavy ions. The later sections of the chapter highlight the results that have been achieved from the XRD and PL measurements of the samples.

5.1 Growth of InGaN/GaN multiple quantum wells

For this study, multiple quantum well (MQW) structures were grown on 430 μm thick c-plane sapphire substrates by metal organic vapor phase epitaxy (MOVPE). Ammonia (NH_3), trimethylindium (TMIn), and trimethylgallium (TMGa) were used as the N, In and Ga source, respectively.

All the samples used in this study consist of a 3 μm thick undoped GaN buffer layer between the substrate and the MQW structure. The famous two-step method has been used in GaN buffer layer growth. This method reduces the amount of dislocations in the buffer layer [39].

Two different series of MQW structures were grown. The series A consisted of 5 quantum wells in the MQW structure and an indium composition of 6% in the active region of the wells. In the series B include the samples have 10 QWs in the MQW structure and the indium composition is around 10%. The main sample properties are

listed in Table 5-1. The temperature during the growth of the active region has been used primarily to control the amount of indium in the wells.

Samples	Number of Wells	Temperature	In composition (%)
Series A	5	790°C	6%
Series B	10	750°C	10%

Table 5-1. Some properties of the sample series.

GaN has been used as a barrier layer with a thickness of 25 nm in all samples. The thickness of the InGaN layers is around 3nm for all the samples. Figure 5-1 shows the simplified form of heterostructures used in this research.

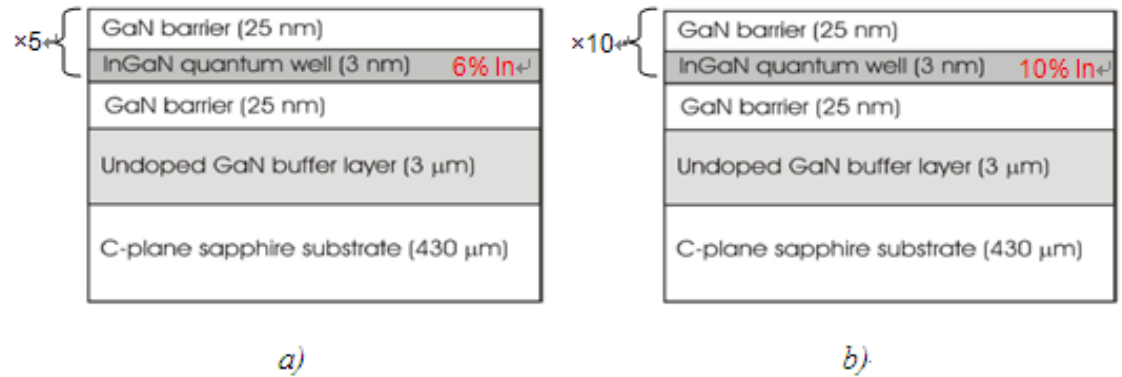


Figure 5-1. Schematic illustration of the sample structure in a) series A having 5 QWs with 6% indium and b) series B having 10 QWs with 10% indium. The MQW structures of all the samples are covered only by the topmost GaN barrier.

5.2 Irradiation by heavy ions

The samples were irradiated with heavy ions having energies below 1MeV/u (mega-electron volt/atomic mass unit) delivered from the 5 MV tandem accelerator based in Uppsala. These irradiations were performed at room temperature under normal incidence with respect to the sample surface. The applied ion fluences were in the range of 10^9 to 10^{12} ions/cm², and homogeneous irradiation over an area of 30x30 mm² was achieved by means of an electrostatic raster scanner. The ion fluence was determined from the irradiation time and the beam current, which was measured using a Faraday cup with 1.0 cm² aperture located behind the sample holder. The energies and ion types used in this study were 13 MeV Br³⁺ and 40MeV I⁹⁺ ions. Computer simulations indicate that both kinds of projectiles completely penetrate the layers of the MQWs in the used samples. The penetration depths in GaN are 3.4 and 6.1 μ m for the used Br and I ions, respectively. Table 5-2 summarizes the sample details and the heavy ion fluences used in the experiments.

Series	Sample structure and composition	Heavy ions and fluence ranges
A	5 QWs 6% Indium in wells	40 MeV I $1.5 \times 10^9 - 6 \times 10^{12}$ ions/cm ² 13 MeV Br $5.6 \times 10^9 - 1.1 \times 10^{11}$ ions/cm ²
B	10 QWs 10% Indium in wells	40 MeV I $1.5 \times 10^9 - 6 \times 10^{12}$ ions/cm ² 13 MeV Br $5.6 \times 10^9 - 1.1 \times 10^{11}$ ions/cm ²

Table 5-2. MQW samples, the bombardment ions and the fluence ranges used in this study.

5.3 XRD results

It has been described in section 4.3.1 that XRD is a powerful tool in determining the quality of the crystal structure of a quantum wells. The $\omega - 2\theta$ XRD scans have been used to analyze the crystal structure of our samples with and without irradiation. Figure 5-2 shows the $\omega - 2\theta$ scan of a 5 QW sample without any irradiation.

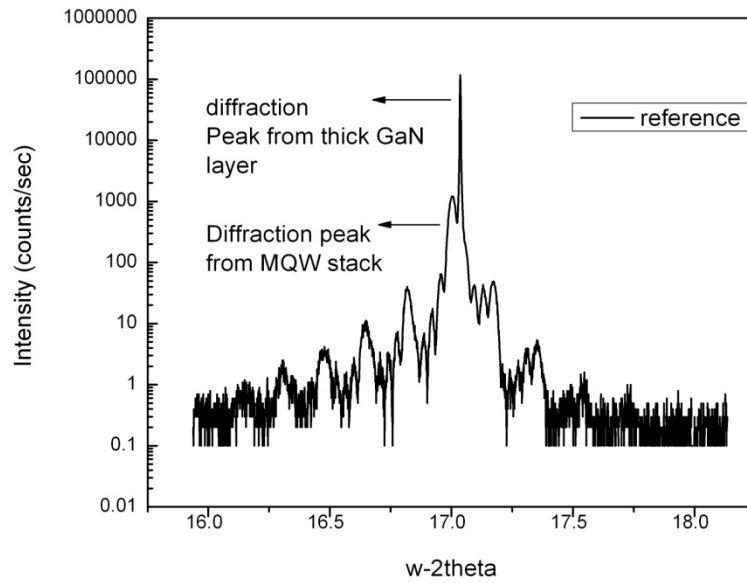


Figure 5-2. The $\omega - 2\theta$ curves of the 5 QW sample (Ref2) without any irradiation.

The sharpest peak in Figure 5-2 comes from the GaN buffer layer. A diffraction peak from the MQW stack can be seen on the left of the GaN peak. Apart from this, there are several sharp satellite peaks that are visible in this curve. The sharpness of these peaks is indicative of the fact that the quality of the interface between individual layers of the structure under investigation is fairly good.

To investigate the effect of the different fluences of either the I^{9+} or Br^{3+} ions, XRD scans were performed on various samples. Figure 5-3 shows the $\omega - 2\theta$ curves of the 5 QW samples with ion fluences ranging between 5.3×10^9 and 6.0×10^{12} ions/cm². The 5 QW reference sample (Ref2) without any irradiation has also been included for easy comparison.

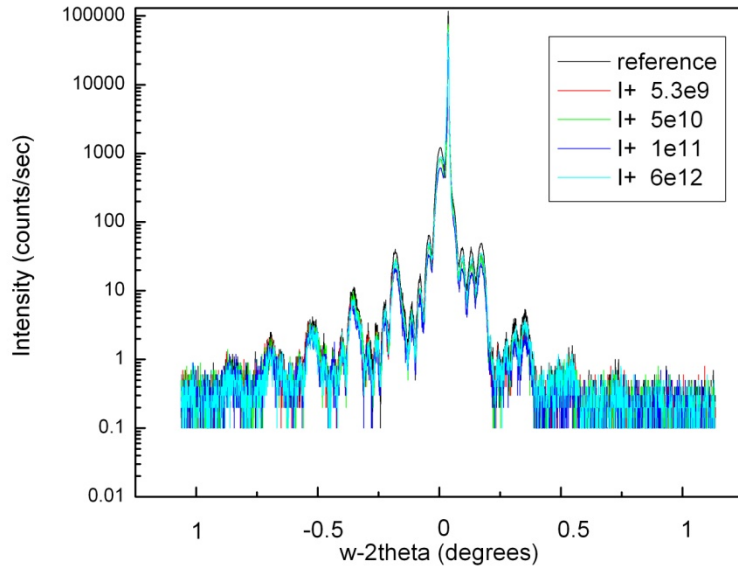


Figure 5-3. $\omega - 2\theta$ curves of the samples which were selected from Series A (5 QWs structure) with different I^{9+} fluencies.

The comparison of XRD scans (Figure 5-3) with various fluences of I^{9+} ions reveals that there has been no major damage to the crystal structure of the MQWs. We have concluded this from the fact that there is no visible change either in the periodicity or the full width half maximum (FWHM) of the diffraction and satellite peaks. This indicates that despite high doses of I^{9+} ions, the crystal structure is intact and the interface quality is still the same as in the sample not exposed to the irradiation.

Similar XRD measurements were performed on the 10 QW samples irradiated with I^{9+} and Br^{3+} ions. The $\omega - 2\theta$ scans of those samples do not differ from that of the reference sample and therefore, no major damage to the crystal structure was observed. It is believed that there might be formation of some point defects (vacancy or interstitial) or small clusters as a result of irradiation. Our XRD results have revealed that it is extremely difficult to observe such defects with $\omega - 2\theta$ scans.

5.4 Continuous wave photoluminescence results

The results obtained from the continuous wave photoluminescence (CW-PL) measurements have been explained below. The measurement results have been categorized according to the irradiation ions in the samples.

5.4.1 CW-PL results of samples irradiated by I^{9+} ions

This section covers the CW-PL results which are obtained from the samples irradiated by 40 MeV I^{9+} ions with fluences in the range of 1.5×10^9 - 6×10^{12} ions/cm². Figure 5-4 shows the room temperature PL spectra of the 5 QW samples irradiated with various fluences of I^{9+} ions. The optical quality of the samples degrades with increasing ion fluence. A fluence of 1.5×10^9 ions/cm² reduces the PL intensity by 30%. When the ion fluence is larger than 5.0×10^{10} ions/cm², the PL intensity is below the background noise level, so the room temperature PL data for such samples has not been included in Figure 5-4.

Figure 5-5 shows the PL spectra of 10 QW samples irradiated with 40 MeV I^{9+} ions. It is clearly evident from the CW-PL spectra that the I^{9+} ions greatly decrease the PL intensity of the samples. A fluence of 1.5×10^9 ions/cm² reduces the PL intensity by 80%. Increasing the I^{9+} ions fluence still decreases the optical quality of the samples. The samples with the ion fluence of 5.0×10^9 ions/cm² or more severely damage the quantum well structure optically. As a result, the PL intensity remains again below the background noise level.

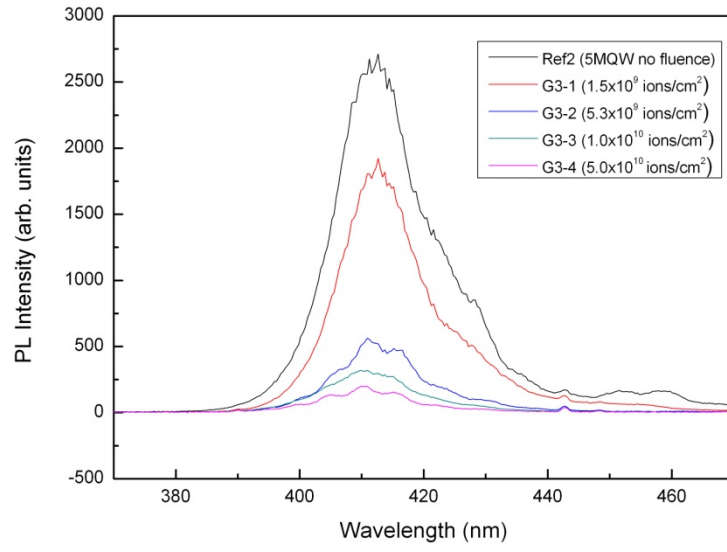


Figure 5-4. PL spectra of the 5 QW samples with different fluences of I^{0+} irradiation.

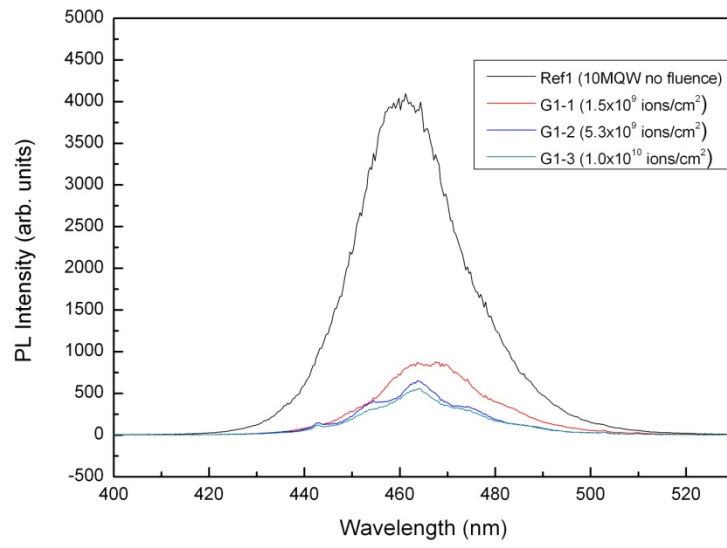


Figure 5-5. PL spectra of the 10 QW samples with different fluences of I^{0+} irradiation.

Figure 5-6 shows, the total integrated area under the PL peak as a function of the fluence of 40MeV I^{9+} ions. The results indicate that the PL intensities from both the 5 and 10 QW structures have a strong dependence on the fluence of iodine ions. The integrated room temperature PL intensity shows that there is a sharper degradation for the 10 QW samples as compared to the 5 QW samples. We believe that the sharp drop of the PL signal in the 10 QW samples as compared to the 5 QW samples could be that an increased amount of indium content in the 10 QW samples causes much more strain in the structure. These strained layers are much easier damaged by irradiation.

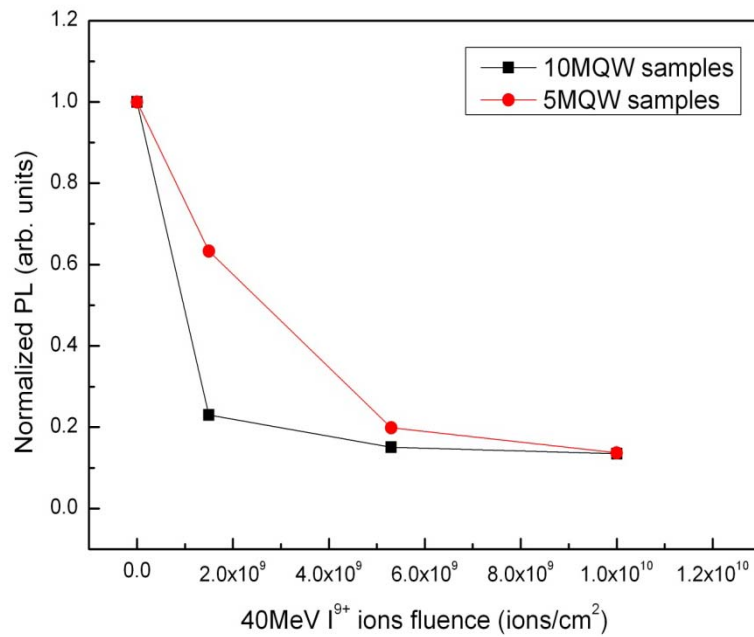


Figure 5-6. Total integrated PL intensity of 5 and 10 QW samples vs. the fluence of 40 MeV I^{9+} ions varying from 1.5×10^9 to 1.0×10^{10} ions/cm². The PL intensity of both the curves has been normalized to one at zero fluence.

5.4.2 CW-PL results of samples irradiated by Br^{3+} ions

The CW-PL results shown in this section have been obtained from the 5 QW and 10 QW samples with 13MeV Br^{3+} ion irradiation. The fluence of Br^{3+} ions ranges from 1.5×10^9 to 6×10^{12} ions/cm². Figure 5-7 shows the room temperature PL spectra of the 5 QW samples irradiated with various fluences of Br^{3+} ions. The optical quality of the samples degrades as the Br^{3+} ion fluence increases.

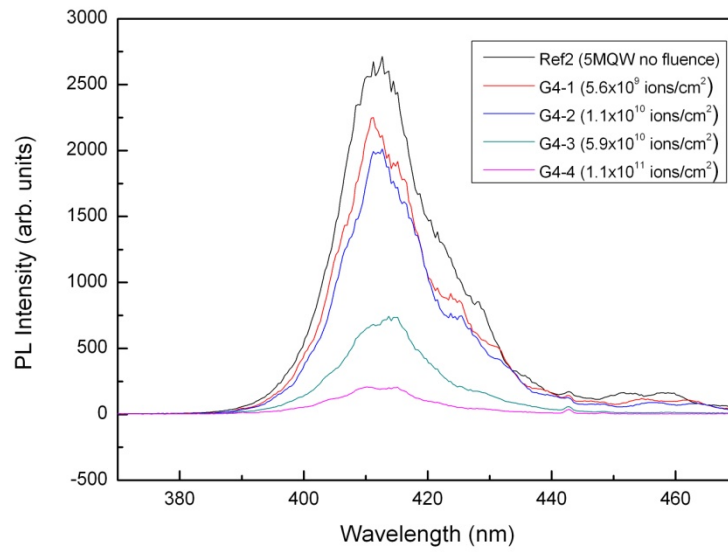


Figure 5-7. PL spectra of the 5 QW samples with different fluences of Br^{3+} irradiation.

Figure 5-8 shows the room temperature CW-PL spectra of 10 QW samples with 13MeV Br^{3+} ion irradiation. It is clearly evident from the PL spectra that the PL intensity decreases with increasing ion fluence.

Figure 5-9 shows the total integrated PL intensity as a function of the fluence of 13 MeV Br^{3+} ions. The results are similar to the samples irradiated with 40 MeV I^{9+} ions. The PL intensities from both the 5 and 10 QW structures strongly depend on the fluence of the Br^{3+} ions. Here again we see that the optical damage caused by the Br^{3+} ions in the 10 QW samples is more severe than in 5 QW samples. It is also noticeable that the

drop in the PL signal is more gradual in both 5 and 10 QW structures irradiated by Br^{3+} ions as compared to I^{9+} ions.

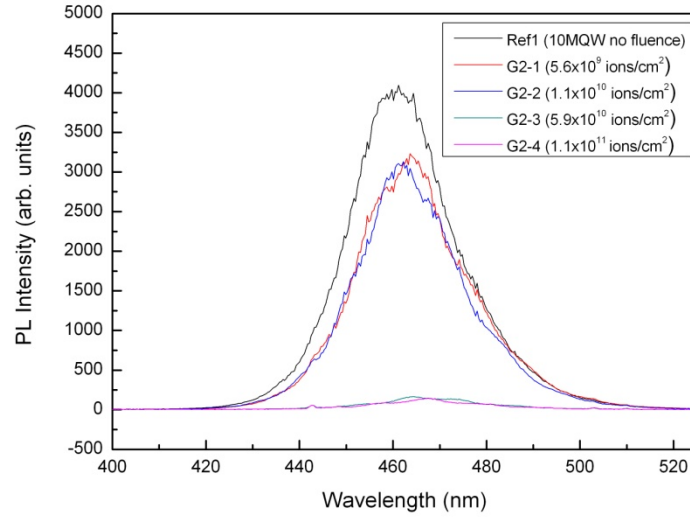


Figure 5-8. PL spectra of the 10 QW samples with different fluences of Br^{3+} irradiation.

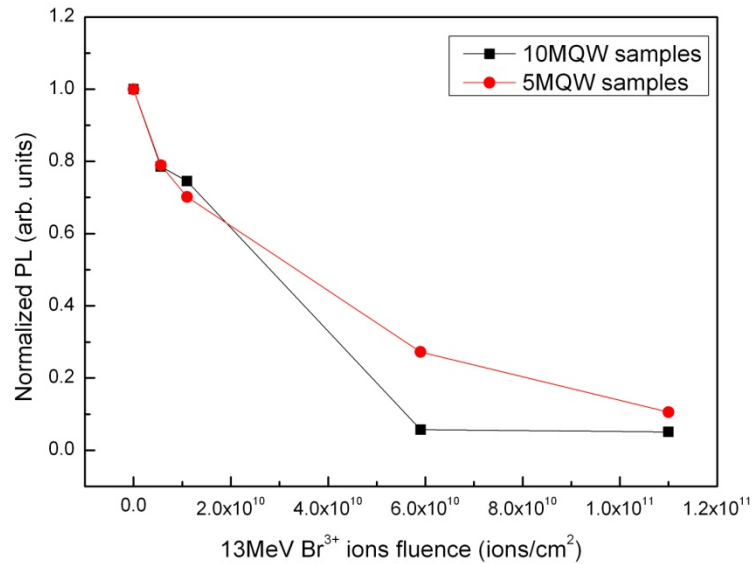


Figure 5-9. Total integrated PL intensity of the 5 and 10 QW samples vs. the fluence of 13 MeV Br^{3+} ions varying from 5.6×10^9 to 1.1×10^{11} ions/cm². Both curves are separately normalized to one at zero fluence.

5.5 Low temperature photoluminescence results

To further extend our investigation, temperature dependent PL measurements were carried out. As we know, the PL intensity gives us information about the radiative and non-radiative recombination rates. A variation of external parameters such as temperature can be used to further characterize the underlying electronic states and energy bands in the material [40]. In this section, we have investigated the effect of radiation on the activation energy and the internal quantum efficiency of the samples.

5.5.1 Activation energy

In our low temperature PL measurement results, the logarithm of the PL intensity vs. the reciprocal of the temperature has been used to study the effect of temperature variation on quantum wells. These graphs often referred to as Arrhenius plots, have been used in previous quantum well studies [41]. Figure 5-10 shows integrated PL intensities irradiated with various fluences of 40 MeV I^{9+} ions. The temperature range used for these experiments is between 15 K and 293 K. It clearly indicates that as the temperature is increasing, the normalized PL intensities of all the samples are reduced. To further characterize the temperature dependent curves shown in Figure 5-10, we use the commonly known Arrhenius equation

$$I(T) = \frac{I_0}{1 + \alpha_1 \exp(-E_{a1} / \kappa_B T) + \alpha_2 \exp(-E_{a2} / \kappa_B T) + \dots} , \quad (5.1) [42]$$

where $I(T)$ is the integrated PL intensity at temperature T , T is the temperature, κ_B is Boltzmann constant, α_i is a constant expressing the recombination probability of process i , E_{ai} is the activation energy of process i and I_0 is the PL intensity at lowest temperature. From the basic principle of activation energy, if the PL measurement temperature is very low (close to 0 K), the electrons and holes that are generated by external light pumping cannot escape from the quantum well. Thus, all the generated electrons and holes recombine in the quantum structures, and the integrated PL intensity

(I_0 which is shown in Eq.5.1) is larger than the one measured at any other temperature. As we move towards higher temperatures, carriers in the quantum structures are affected by the thermal activation energy, and they start to escape from the wells, and the PL intensity drops [43]. The estimated activation energies of the InGaN/GaN 5 QW and 10 QW samples with different fluences of I^{9+} ions are shown in Table 5-3.

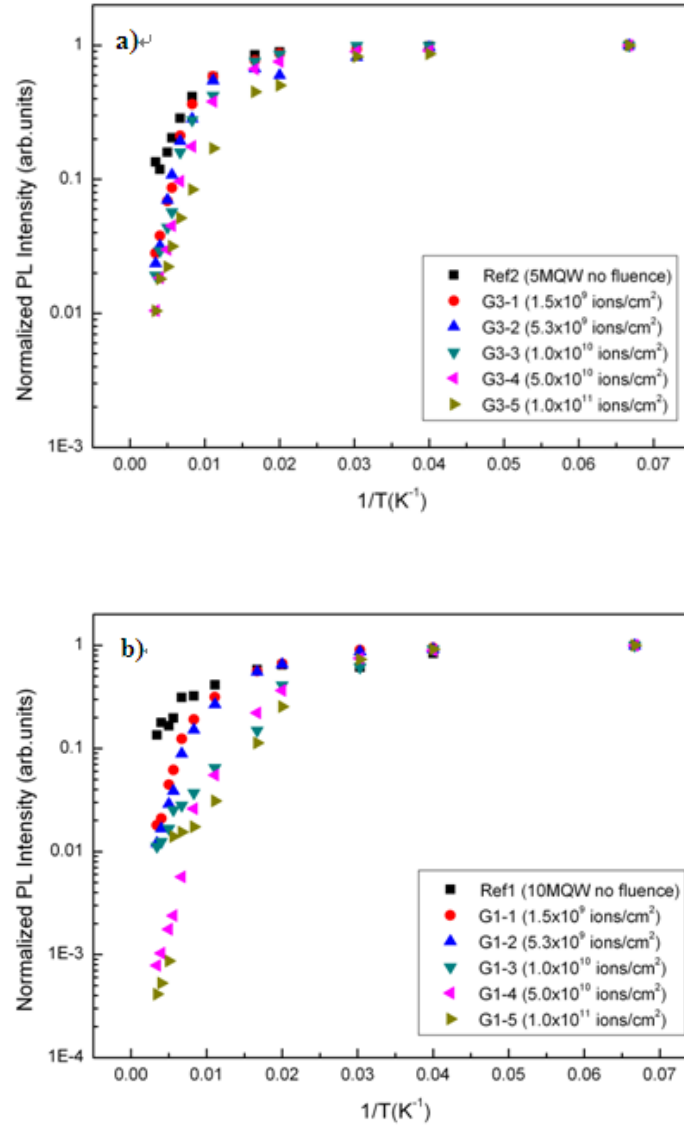


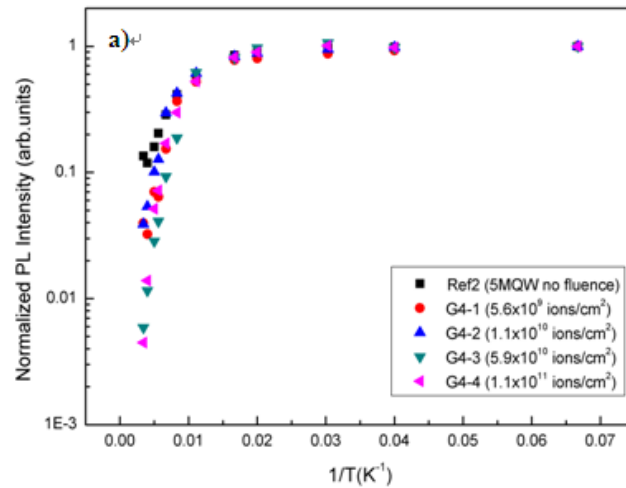
Figure 5-10. Arrhenius plots of integrated PL intensities for InGaN/GaN QW samples with a) 5 QWs and b) 10 QWs as a function of the fluence of I^{9+} ion irradiation. All the curves are separately normalized to one at the lowest temperature.

Samples (5 QWs)	Estimated activation energies (meV)		Samples (10 QWs)	Estimated activation energies (meV)	
	E_{a1}	E_{a2}		E_{a1}	E_{a2}
Ref2 (no fluence)	30.5	104.0	Ref1 (no fluence)	32.1	102.0
G3-1(1.5×10^9 ions/cm ²)	28.9	89.0	G1-1(1.5×10^9 ions/cm ²)	31.4	86.2
G3-2(5.3×10^9 ions/cm ²)	26.5	73.3	G1-2(5.3×10^9 ions/cm ²)	29.9	76.0
G3-3(1.0×10^{10} ions/cm ²)	24.4	66.1	G1-3(1.0×10^{10} ions/cm ²)	22.9	60.1
G3-4(5.0×10^{10} ions/cm ²)	22.6	57.5	G1-4(5.0×10^{10} ions/cm ²)	20.6	49.1
G3-5(1.0×10^{11} ions/cm ²)	17.3	50.6	G1-5(1.0×10^{11} ions/cm ²)	17.6	39.2

Table 5-3. Estimated activation energies in the 5 QW and 10 QW samples with different I^{9+} ion fluences.

Table 5-3 clearly shows that the energy levels seen in Ref 1 and Ref 2 samples are the same. We believe that in the irradiated samples there are more than 2 levels as the activation energy is changing continuously. It means that the irradiation is creating shallow levels. These shallow levels are not related to yellow luminescence, which originates from deeper levels.

The integrated PL intensities of the 5 and 10 QW samples irradiated with 13 MeV Br^{3+} ion and the estimated activation energies are shown in Figure 5-11 and Table 5-4, respectively.



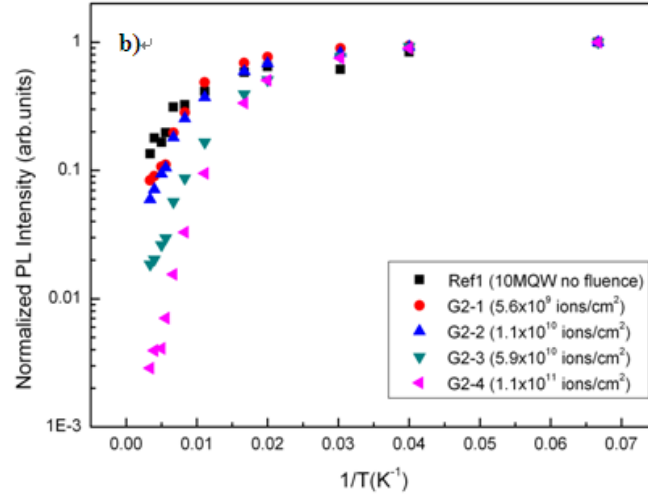


Figure 5-11. Arrhenius plots of integrated PL intensities for InGaN/GaN QW samples with a) 5 QWs and b) 10 QWs as a function of the fluences of Br^{3+} ion irradiation. All the curves are separately normalized to one at the lowest temperature.

Samples (5 QWs)	Estimated activation energies (meV)		Samples (10 QWs)	Estimated activation energies (meV)	
	E_{a1}	E_{a2}		E_{a1}	E_{a2}
Ref2 (no fluence)	30.5	104.0	Ref1 (no fluence)	32.1	102.0
G4-1(5.6×10^9 ions/cm ²)	27.6	90.0	G2-1(5.6×10^9 ions/cm ²)	30.5	95.1
G4-2(1.1×10^{10} ions/cm ²)	26.1	74.2	G2-2(1.1×10^{10} ions/cm ²)	28.5	78.1
G4-3(5.9×10^{10} ions/cm ²)	24.6	61.0	G2-3(5.9×10^{10} ions/cm ²)	23.3	58.3
G4-4(1.1×10^{11} ions/cm ²)	23.3	95.5	G2-4(1.1×10^{11} ions/cm ²)	21.9	48.3

Table 5-4. Estimated activation energies in the 5 QW and 10 QW samples with different Br^{3+} ion fluences.

5.5.2 Internal quantum efficiency

The temperature dependent photoluminescence (PL) was used to determine the internal quantum efficiency (IQE) of the QW structures. At very low temperatures the non-radiative recombination is close to minimum and radiative recombination processes are dominant. With increasing temperature, non-radiative recombination processes get activated and play a key role at room temperature [44]. Figure 5-12 shows the IQE of samples with different irradiation fluencies calculated from

$$IQE = \frac{PL_{300K}}{PL_{15K}}, \quad (5.2)$$

where PL_{300K} is the PL intensity at room temperature and PL_{15K} is the PL intensity at the lowest temperature in our system.

The IQE of the samples irradiated with 40 MeV I^{9+} ions declines severely, which is shown in Figure 5-12 a). From Figure 5-12 b), we find that the decrease of the IQE in the samples irradiated with Br^{3+} ions is not as sharp as that in samples irradiated with I^{9+} ions. The possible reason can be the different nature of the Br^{3+} ions as compared to I^{9+} . As was mentioned in section 4.2.3, the Br^{3+} ions may create isolated point defects and I^{9+} ions result small clusters of point defects or just large concentration of isolated point defects. That is why the damage done to the samples are different in the case of different ions.

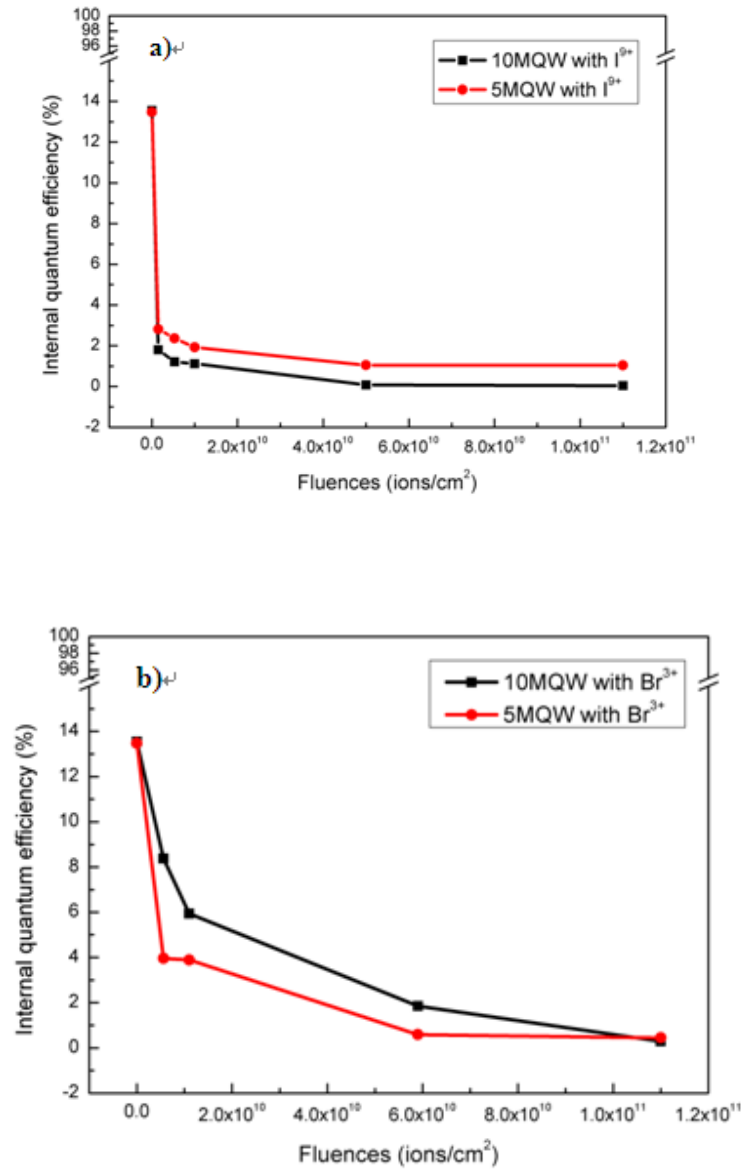


Figure 5-12. Internal quantum efficiency of a) 5 QW and 10 QW samples irradiated by 40MeV I⁹⁺ ions and b) 5 QW and 10 QW samples irradiated by 13MeV Br⁹⁺ ions as a function of irradiation fluence.

5.6 Time resolved photoluminescence at room temperature

The time resolved photoluminescence (TR-PL) measurement method was introduced in Section 4.3.2. TR-PL measurements were performed on a few 10 QW samples irradiated with different fluences. The decay time τ_i is determined from the TR-PL transients by fitting [45,46]

$$I(t) = A_1 \exp(-t/\tau_1) + A_2 \exp(-t/\tau_2) + C \quad , \quad (5.3)$$

where $I(t)$ is PL intensity, A_i is constant, t is the pulse scanning time, τ_i is the carrier lifetime (PL decay constant) given by

$$\frac{1}{\tau_i} = \frac{1}{\tau_R} + \frac{1}{\tau_{NR}} \quad , \quad (5.4)$$

where τ_R is the lifetime of the radiative carriers and τ_{NR} is the lifetime of the non-radiative carriers. Table 5-5 shows the calculated decay times from three different samples and Figure 5-13 shows the measured PL intensity decay of these samples.

Samples (10 QWs)	Fluences of I^{9+} ions (ions/cm ²)	τ_1 (ns)	τ_2 (ns)
Ref1	None	31.13	3.49
G1-2	1.5×10^9	8.01	3.43
G1-5	1.0×10^{11}	1.18	3.25

Table 5-5. Decay times of the samples.

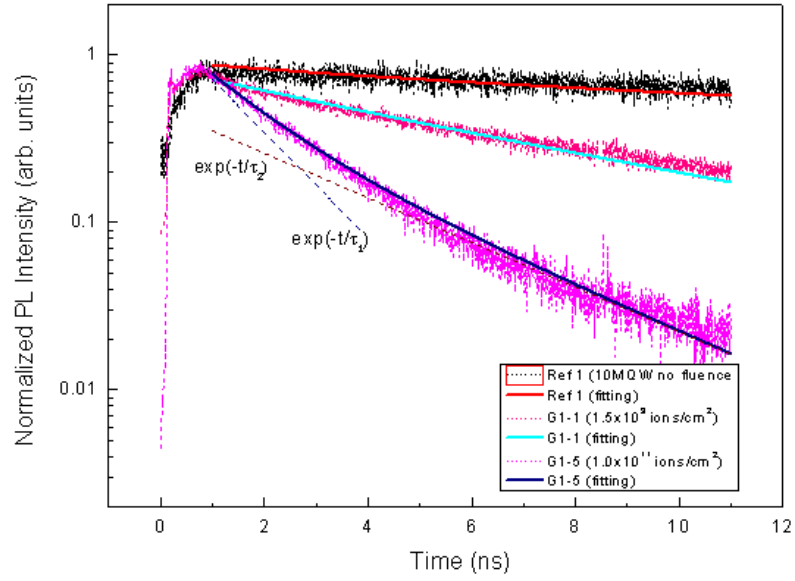


Figure 5-13. Time dependent PL intensity of the samples with different fluences of I^{9+} ion irradiation.

It can be clearly seen that the decay time τ_1 has notably decreased with the increase of I^{9+} fluence, while τ_2 is almost unchanged. The reason for the decrease in the decay time with the increase of ion fluence could be the formation of localized point defects which act as non-radiative recombination centers. The unchanged value of τ_2 indicates that it is related to a process not affected by irradiation. Because the time constant τ_2 is so large, the process can be related to spatial carrier separation by, e.g., the polarization field.

6 Summary

The properties of irradiated InGaN/GaN multiple quantum wells have been studied by XRD and PL techniques. MQW structures with different indium compositions and different number of QWs were grown by MOVPE. The irradiation of quantum wells was performed at room temperature with two different heavy ions (Br^{3+} and I^{9+}). The fluences of these ions were varied from 10^9 to 10^{12} ions/cm².

The XRD rocking curves indicated that there has been no major damage to the overall crystal structure of the quantum well samples. Even the samples with a very high fluence of ions give no change in the FWHM or periodicity of the diffraction and satellite peaks. We believe that the extent of the damage is very small and it is not possible to observe the damage by XRD.

The PL measurements show that the optical properties of the samples irradiated with both ions have a strong dependence on the fluences of heavy ions. The continuous wave photoluminescence results at room temperature indicate that there is a sharp degradation for samples irradiated with I^{9+} ions with increasing fluence. It is also noticeable that the drop in the PL signal is more gradual in samples irradiated with Br^{3+} ions as compared to I^{9+} ions. This phenomenon can be caused by the fact that bromine ion is lighter than iodine ion. Also the energy of the bromine ion is lower than that of the iodine ion.

The low temperature PL measurement results clearly indicate that as the temperature is increasing, the PL intensities of all the samples are reduced. The activation energy and

internal quantum efficiency of the samples also show a similar dependence on the fluence of irradiation.

Due to the pump laser wavelength (around 400 nm), only 10 QW samples have been studied in the time resolved PL measurement. The results show that the decay time decreased significantly with the increase of heavy ion fluence. From the results of all three types of PL measurements that were performed in the course of this research work, it is believed that localized defects were created as a result of irradiation. The defects could be point defects, Frenkel pairs, or small clusters of such defects.

For future work, transmission electron microscopy (TEM) should be used to study the exact nature of the defects. High resolution TEM images can reveal the type and extent of the damage caused in the quantum wells.

Appendix 1

Catalog of measured InGaN/GaN samples

Sample name	Description	Fluence
Ref1	10 QWs, without irradiation	no fluence
Ref2	5 QWs, without irradiation	no fluence
G1-1	10 QWs, irradiated by 40MeV I ⁹⁺	1.5×10^9 ions/cm ²
G1-2		5.3×10^9 ions/cm ²
G1-3		1.0×10^{10} ions/cm ²
G1-4		5.0×10^{10} ions/cm ²
G1-5		1.0×10^{11} ions/cm ²
G1-6		1.1×10^{12} ions/cm ²
G1-7		6.0×10^{12} ions/cm ²
G2-1	10 QWs, irradiated by 13MeV Br ³⁺	5.6×10^9 ions/cm ²
G2-2		1.1×10^{10} ions/cm ²
G2-3		5.9×10^{10} ions/cm ²
G2-4		1.1×10^{11} ions/cm ²
G3-1	5 QWs, irradiated by 40MeV I ⁹⁺	1.5×10^9 ions/cm ²
G3-2		5.3×10^9 ions/cm ²
G3-3		1.0×10^{10} ions/cm ²
G3-4		5.0×10^{10} ions/cm ²
G3-5		1.0×10^{11} ions/cm ²
G3-6		1.1×10^{12} ions/cm ²
G3-7		6.0×10^{12} ions/cm ²
G4-1	5 QWs, irradiated by 13MeV Br ³⁺	5.6×10^9 ions/cm ²
G4-2		1.1×10^{10} ions/cm ²
G4-3		5.9×10^{10} ions/cm ²
G4-4		1.1×10^{11} ions/cm ²

Appendix 2

Fitting curves for the determination of activation energies

Figure A and B show the curves obtained by fitting the data points with Arrhenius Formula

$$I(T) = \frac{I_0}{1 + \alpha_1 \exp(-E_{a1} / \kappa_B T) + \alpha_2 \exp(-E_{a2} / \kappa_B T) + \dots},$$

Where $I(T)$ is the integrated PL intensity at temperature T , T is the temperature, k_B is Boltzmann constant, E_a is equal to the activation energy and I_0 is the PL intensity at lowest temperature.

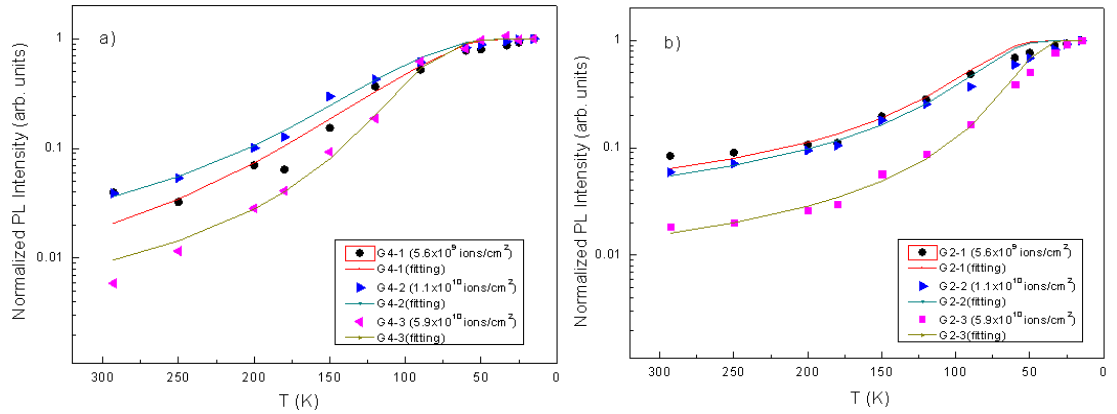


Figure A. Fitting curves for the samples irradiated with 13MeV Br^{3+} ions.

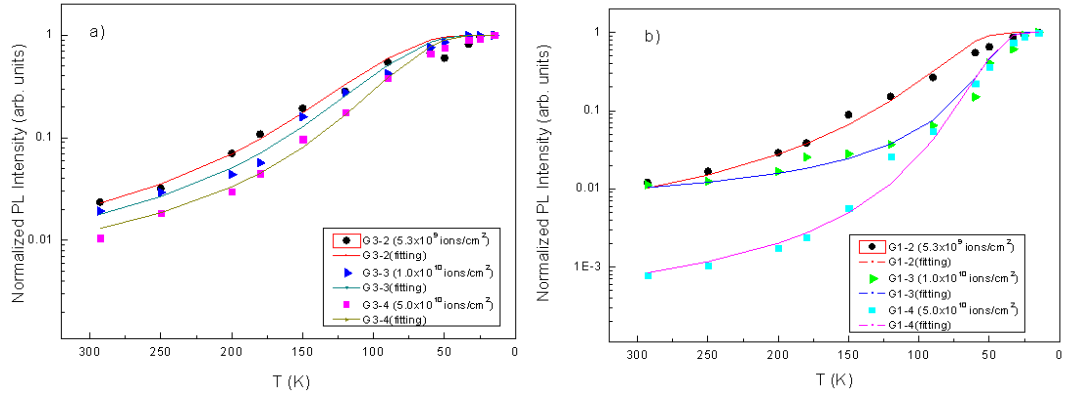


Figure B. Fitting curves for the samples irradiated with 40MeV I^{9+} ions

References

- [1] J. Grant, R. Bate, W. Cunningham, GaN UV detectors for protein studies, Nuclear Instruments and Methods in Physics Research A 563 (2006) 27 – 30.
- [2] R.A. Smith, Semiconductor, 2nd ed., Cambridge Univ. Press, London, 1979.
- [3] S.M. Sze, Semiconductor Devices Physics and Technology, 2nd ed., Wiley, New York, 2001.
- [4] M. Mansfield, C. O’Sullivan, Understanding Physics, Wiley, New York, 1998.
- [5] J. Singh, Semiconductor Optoelectronics Physics and Technology, McGraw-Hill International Editions, 1995.
- [6] <http://micro.magnet.fsu.edu/primer/lightandcolor/ledsintro.html>
- [7] H.P. Myers, Introductor Solid Sate Physics, Taylor and Francis London, 2nd edition, 1997.
- [8] P. Kuivalainen, Physical Modeling of Semiconductor Devices, TKK, Espoo, 2006.
- [9] M. Ali, MOVPE Growth of InAlGa_N Layers and Quantum Structures for UV Applications, Master thesis, TKK, Espoo, 2007.
- [10] <http://photon.soe.ucsc.edu/intersubband.html>
- [11] P. Harrison, Quantum Wells, Wires and Dots, Wiley, New York, 2000.
- [12] T. Böttcher, Hetero-epitaxy of group III nitrides for the applications in laser diodes, dissertation, University of Bremen, 2002.
- [13] S. Muraleedharan, Processing of Gallium Nitride Blue Light Emitting Diode Chips, Master thesis, TKK, Espoo, 2007.
- [14] J. H. Edger , Properties, Processing and Applications of Gallium Nitride and Related Semiconductors, INSPEC, London, 1999
- [15] R. W. G Wyckoff, Crystal Structures vol. 1, Wiley, New York, 1965.
- [16] H. Schulz, K.H. Thiemann, Solid State Commun. (USA) vol.23 (1977) p.815
- [17] S. Nakamura, G. Fasol, The blue laser diode, Springer Verlag, Berlin, 1997.
- [18] <http://www.emf.co.uk/>
- [19] J.J. Coleman, Proceedings of IEEE. 85, 1715-1729, 1997.
- [20] R. Steins, New Process Approaches to Metalorganic Vapor Phase Epitaxy of III-nitrides for High Power HEMTs, Dissertation, 2006.

-
- [21] M. A. Herman, W. Richter and H. Sitter, Epitaxy, Physical Principles and Technical Implementation, Springer- Verlag, 2004.
- [22] C.Claeys, E. Simoen, Radiation Effects in Advanced Semiconductor Materials and Devices, Springer, 2002
- [23] C. Leroy, P.G. Rancoita, Particle Interaction and Displacement Damage in Silicon Devices Operated in Radiation Environment, Rep. Prog. Phys.70 (493-625) 2007.
- [24] M. J. Beck, R. Hatcher, L Tsetseris, M Caussanel, Elemental Defect Processes in Radiation Induced Displacement Damage in Si, 2006 MURI Review, 2006.
- [25] J. R. Sroufe, IEEE transactions on nuclear science, Vol. 50, No. 3, 2003.
- [26] A. K. Sutton, Displacement Damage and Ionization Effects Advanced Silicon-Germanium Heterojunction Bipolar Transistors.
- [27] Radiation Protection for Particle Accelerator Facilities, NCRP, (Report No. 144), 2003.
- [28] V. D .S. Dhaka, N. V Tkachenko, H. Lemmetyinen, Effects of heavy-ion and light-ion irradiation on the room temperature carrier dynamics of InGaAs/GaAs quantum wells, Semicond. Sci. Technol. 21 (2006) 661-664.
- [29] L. Joulaud, J. Mangeney, Thermal stability of ion-irradiated InGaAs with (sub-) picoseconds carrier lifetime, Appl. Phys. Lett. 2003.
- [30] J. Mangeney, J. Lopez, N. Stelmakh, J. M. Lourtioz, J.L. Oudar, H. Bernas, Subgap optical absorption and recombination center efficiency in bulk GaAs irradiated by light or heavy ions, Appl. Phys. Lett. 76, 40 (2000).
- [31] J. Mangeney, H. Choumane, G. Patriarche, G. Leroux, G. Aubin, J.C. Harmand, J. L. Oudar, H. Bernas, Comparison of light- and heavy-ion-irradiated quantum-wells for use as ultrafast saturable absorbers, Appl. Phys. Lett. 79, 2722 (2001).
- [32] K. Nordlund, J. Peltola, J. Nord, J. Keinonen, and R. S. Averback, Defect clustering during ion irradiation of GaAs: a molecular dynamics study, J. Appl. Phys. 90, 1710 (2001)
- [33] N. A. Sanford, A. Munkholm, M. R. Krames, Refractive index and birefringence of $\text{In}_x\text{Ga}_{1-x}\text{N}$ films grown by MOCVD, phys. stat. sol. (c) 2, No. 7, 2783–2786, 2005
- [34] B.D. Cullity, S.R. Stock, Elements of X-ray Diffraction (3th ed), Prentice Hall, 2001.

-
- [35] S. Suihkonen, Fabrication of InGaN Quantum Wells for LED Application, Doctoral Dissertation, Espoo, 2008.
- [36] A.Y. Cho, Molecular Beam Epitaxy, AIP Press, New Jersey, 1994.
- [37] T.H. Gfroerer, Photoluminescence in Analysis of Surfaces and Interfaces, John Wiley, New York, 2000.
- [38] L.W. Molenkamp, H.F.J. Van't Blik, Very Low Interface Recombination Velocity in (Al,Ga) As Heterostructures Grown by Organometallic Vapor-phase Epitaxy, J.Appl. Phys., 65, 4253-4256 (1988).
- [39] I. Akasaki, H. Amano, Y. Koide, K. Hiramatsu, N. Sawaki, J. Cryst. Growth. 98.209-219, (1989).
- [40] T. Gfroerer, Photoluminescence in Analysis of Surface and Interfaces, Encyclopedia of Analytical Chemistry.
- [41] Z. Zhu, H. Yoshihara, K. Takebayashi, T. Yao, Characterization of Alloy Formation at the ZnSe/CdSe Quantum-well Interface by Photoluminescence Spectroscopy, J. Cryst. Growth, 138, 619–624 (1994).
- [42] B.Schineller, P.H. Lim, G.P. Yablonskii, E.V. Lutsenko, Characterization of Undoped and Silicon-Doped InGaN/GaN Single Quantum wells, Journal of ELECTRONIC MATERIALS, Vol.29, No. 1, 2000.
- [43] J. S. Kim, E. K. Kim, Study on the Energy-Band Structure of an InAs/InGaAs/GaAs Quantum-Dot Infrared Photodetector Structure, 2006.
- [44] D. Fuhrmann, Optimizing the internal quantum efficiency of GaInN SQW structures for green light emitters, phys.stat.sol.(c)3, 2006
- [45] W. Shockley, Electrons and Holes in semiconductors, Van Nostrand, New York, 1950.
- [46] J. Dreybrodt, F. Daiminger, J.P. Reithmaier, A. Forcel, Phys, Rev B 51, 1995.